arXiv:1603.03266v1 [quant-ph] 10 Mar 2016

Topological Phenomena in Classical Optical Networks

T. Shi[1], H. J. Kimble[1,2,3], and J. I. Cirac[1]

[1] *Max-Planck-Institut für Quantenoptik, Hans-Kopfermann-Str. 1, 85748 Garching, Germany*
[2] *Norman Bridge Laboratory of Physics 12-33*
[3] *Institute for Quantum Information and Matter, California Institute of Technology, Pasadena, CA 91125, USA*

We propose a scheme to realize a topological insulator with optical-passive elements, and analyze the effects of Kerr-nonlinearities in its topological behavior. In the linear regime, our design gives rise to an optical spectrum with topological features and where the bandwidths and bandgaps are dramatically broadened. The resulting edge modes cover a very wide frequency range. We relate this behavior to the fact that the effective Hamiltonian describing the system's amplitudes is long-range. We also develop a method to analyze the scheme in the presence of a Kerr medium. We assess robustness and stability of the topological features, and predict the presence of chiral squeezed fluctuations at the edges in some parameter regimes.

Introduction.—The discovery of topological insulators (TI), as well as Quantum Spin Hall (QSH) insulators [1–9] have opened up a wide range of scientific and technological questions. Their spectra (dispersion relation) feature a set of bands, connected by chiral edge modes that reflect the topological nature of the material. These modes are robust against perturbations whose energy does not exceed the corresponding bandgap and that do not break the time-reversal (TR) symmetry, in the case of the QSH [10, 11]. Electronic interactions give rise to a wide range of phenomena. Although the edge modes persist, their properties are qualitatively modified [12]. In addition, they can give rise to other exotic phenomena, like the fractionalization of charges, or the appearance of excitations with fractional statistics [13, 14].

Recent proposals to generate TI and QSH with (classical) light have also attracted a lot of attention [15–28]. In fact, the first experimental observations [15, 16] of topological features in optical systems have been recently reported, and a several schemes exhibiting intriguing features have been proposed [17–25]. There exist different setups where one can realize the optical analog of QSH, and observe similar features. In the context of coupled resonator arrays, one can use either differential optical paths in waveguides [26] or an optical active (Faraday rotator) element [27]. Despite their success, in the first case it would be desirable to enlarge the bandgaps in the spectrum, which is limited by the small coupling of the local modes in the (high finesse) resonators [26], in order to gain robustness. In the second, photon absorption in the active media also limits the operationality of the scheme. In other schemes, like the one based on bianisotropic metacrystals [28], the realization of long-lived edge modes in a broader frequency range is challenged by the weak bianisotropy in metamaterials [29, 30]. The effects of interactions in those optical models have been scarcely investigated [24, 31, 32]. In particular, the fate of the edge modes, their stability, or the appearance of quantum features has not been analyzed so far.

In this letter we propose and analyze a scheme to realize the optical version of the QSH insulator, and investigate the effects produced by Kerr-nonlinearities, which play the role by photon-photon interactions. Our scheme uses beam splitters, lambda plates, and birrefringent materials, that are optically passive and thus circumvent the problem of photon absorption. In contrast to previous schemes, the effective Hamiltonian description of our setup features long-range hopping behavior, which dramatically broadens the spectral bands and bandgaps,

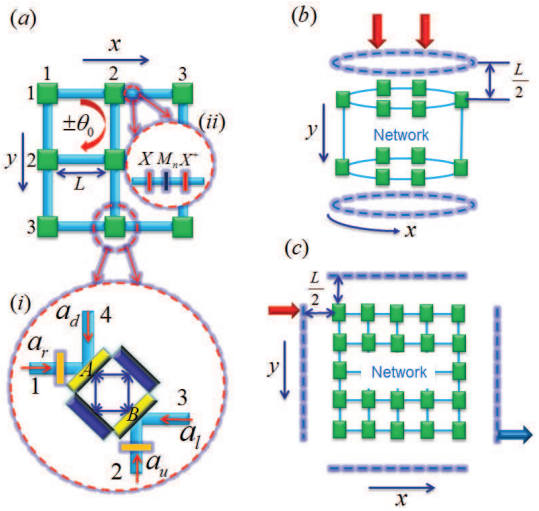

FIG. 1: (Color Online) Schematic of our optical network: (a) Two insets show the construction of optical elements in nodes and fibers, respectively. Here, the light acquires a polarization-dependent phase θ_0 by propagating clockwise around each plaquette (the red arrow). (b)-(c) Perfect and partially transmissive mirrors are put along the boundaries of the cylindrical and planar networks. Here, the partially transmissive mirrors are placed along the top boundary in the cylindrical network, and at the top-left and bottom-right corners in the planar network. The driving light (red arrows) is applied to generate the bulk and edge excitations, and the transmitted light is denoted by the blue arrow. Detailed descriptions of the various elements are given in Ref. [33].

thus adding robustness to perturbations. In fact, the edge modes cover a large frequency range. They can be excited with optical driving, and detected through the measurement of phase shifts and the transmission spectrum. In the presence of a Kerr medium, the chiral edge modes survive, can be externally excited, and are stable in some parameter regimes which we identify. By additionally probing with a different light frequency, edge (Bogoliubov) excitations can be excited. As an interplay between the Kerr-nonlinearity and the topology, they are also chiral and possess quantum features, namely they are squeezed. In order to obtain these results, we develop a scattering matrix approach, and show how to solve it with numerical methods.

Model setup.—The architecture of the non-trivial topology is designed in the 2D network with size $N_x \times N_y$ by the linear optics elements, i.e., optical fibers, birefringent elements, beamsplitters and perfect mirrors. As shown in Fig. 1, at each node of a square lattice, two beamsplitters with reflectance $R_{\rm bs} = (\sqrt{2}-1)^2 \sim 0.17$ and two perfect mirrors form a "bad cavity" to change the propagation direction of the light, and nearest neighbor nodes are connected by one optical fiber with length L. The inset (i) in Fig. 1a shows that the fibers 1 and 4 are connected to the beamsplitter A, while the fibers 2 and 3 are connected to the beamsplitter B. Two birefringent elements next to the node in the fibers 1 and 2 cancel the sign change of the vertical polarization for the light propagating through the node (Sec. I in [33]).

The inset (ii) in Fig. 1a shows that in each horizontal fiber, three birefringent elements are applied to generate an artificial "magnetic" field for the light propagating in the network. From left to right, the three birefringent elements are described by the Jones matrices $X = e^{i\pi\sigma_x/4}$, $M_n = e^{in\theta_0\sigma_z}$, and $X^\dagger$ defined in the linear polarization basis (H, V), where $\sigma_{x,y,z}$ are Pauli matrices, and the phase shift $n\theta_0$ depends on the row index n. The interaction of photons is induced by a Kerr nonlinearity in the fiber, where the light propagating in the fiber acquires an additional phase proportional to the light intensity.

Different boundary conditions give rise to a rich variety of geometries for the network. As shown in Figs. 1b and 1c, for the cylindrical and planar geometries, perfect mirrors are placed along the boundaries to form the closed network, where the distance between boundary mirrors and boundary nodes is $L/2$. In the open network with partially transmissive mirrors on the boundary, nontrivial topological states can be generated and detected by external fields injected through the boundary mirrors.

Linear Regime.— The birefringent elements cause the light to acquire a phase matrix $\theta_0\sigma_y$ by propagating around each plaquette. Hence, the system is TR-invariant, namely, circular polarizations ($\sigma_\pm$) experience oppositely directed "magnetic" fields with fluxes $\pm\theta_0$, respectively, which is the origin of nontrivial topology in the network of linear optical elements.

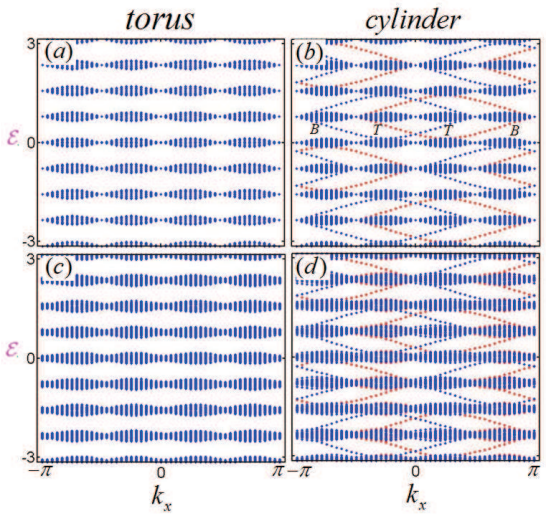

FIG. 2: (Color Online) The energy spectra on the torus and cylinder, where $\theta_0 = \pi/2$, the network size is 48×48, and L is taken as unit. The blue and red colors denote σ_+ and σ_- polarizations, respectively. (a)-(b) The energy spectrum $\mathcal{E}$ on the torus (a) and the cylinder (b) without phase randomness and zero losses of linear elements, where B and T denote the bottom and top boundaries, respectively. (c)-(d) The energy spectrum Re$\mathcal{E}$ on the torus (c) and the cylinder (d) with phase randomness and nonzero losses of linear elements.

The photonic spectra $\mathcal{E}$ of linear network with different geometries display non-trivial topologies of the light, which are determined by the scattering equation $S_0\Psi_{nm} = e^{-i\mathcal{E}L}\tilde{\Psi}_{nm}$ (Sec. IIA and III in [33]). Here, the free S-matrix S_0 connects the right-, up-, left-, and down-moving input fields $\Psi_{nm} = (a_{r,nm}, a_{u,nm}, a_{l,nm}, a_{d,nm})^T$ at the node (n, m) with the input amplitudes $\tilde{\Psi}_{nm} = (a_{r,nm+1}, a_{u,n-1,m}, a_{l,nm-1}, a_{d,n+1m})^T$ at four nearest neighbor nodes. The eigenmode has the definite σ_+ or σ_- polarization due to the block structure of S_0 in the basis of circular polarizations. Figures 2a-b show the spectra of networks on the torus and the cylinder in one period $\mathcal{E} \in \omega_c + (-\pi/L, \pi/L]$ around a large central frequency $\omega_c = 2\pi N_c/L$ (N_c is an integer), where $\theta_0 = \pi/2$, and k_x is the quasi-momentum of the eigenmode $a_{(r,u,l,d),nm} = a_{(r,u,l,d),n}e^{ik_x m}/\sqrt{N_x}$.

As shown in Fig. 2a, for the torus geometry, the photonic bands with broad gaps span across the whole spectral period $2\pi/L$. In contrast with narrow-band schemes [26, 27], the wide spectrum results from the large hopping strength (comparable with $2\pi/L$) between nodes (i.e., cavities) beyond nearest neighbors in the "bad cavity" regime $R_{\rm bs} \sim 0.17$. This long-range hopping behavior is characterized by the spatially nonlocal Hamiltonian $H_{\rm eff} = i\ln S_0/L$ rather than the Hofstadter (tight binding) model [34].

As a consequence of the bands with the non-trivial Z_2 topological index [10], the helical edge modes arise

in the broad topological band gaps. In Fig. 2b, for the cylindrical geometry, the spectrum displays the four edge modes between band gaps, where the chiralities of two edge modes on each boundary are locked to the $\sigma_\pm$ polarizations. The topologically protected helical edge modes are immune to any local perturbation, randomness, and losses, as long as the band gap remains open. Figures 2c-d show that for the random phase fluctuation $\delta_p \in [-0.2, 0.2]$ around $\theta_0 = \pi/2$ and the optical losses (10%) of each element, the band gaps in the energy spectrum Re$\mathcal{E}$ are still opened on the torus, and the helical edge modes survive on the cylinder with a long life-time $\tau = 1/\mathrm{Im}\mathcal{E} \sim 13L$ (the speed c of light is taken as the unit).

In order to generate and probe the edge and bulk modes, input light $A^{(0)}_{\mathrm{in},m}e^{-i\omega_\mathrm{d}t}$ with amplitude $A^{(0)}_{\mathrm{in},m} = A^{(0)}_{\mathrm{in}}e^{ik_x m}/\sqrt{N_x}$ and frequency ω_d is applied to drive the cylindrical network (Fig. 1b) through each of the transmissive top-boundary mirrors with the reflection coefficient r_BM. Significantly, the relative phase shift $\Delta - (\pi + 2\arctan r_\mathrm{BM}) \in (-\pi, \pi]$ (Sec. IIIB in [33]) of reflected light from the network jumps from $-\pi$ to π, when ω_d sweeps across a resonant frequency $\mathcal{E}$ of the closed network. Thus, the measurement of this phase shift reveals the spectrum. As shown in Fig. 3a, for σ_+ polarized driving light, the peaks of $d\Delta/d\omega_\mathrm{d}$ show the band structure and the chiral edge mode on the top boundary. Since the bottom edge mode decays exponentially along the y-direction, its decoupling to the driving light makes the bottom edge mode invisible in Fig. 3a, which isolates a single σ_+ polarized chiral edge mode on the top boundary.

For the planar network, the circularly polarized driving light with amplitude $A^{(0)}_\mathrm{in}$ and frequency ω_d is injected through the transmissive mirror at the upper-left corner (Fig. 1c). As shown in Fig. 3b, the transmission spectrum of output light through the mirror at the bottom-right corner displays the energy spectrum of the planar network. For $\omega_\mathrm{d} \sim 0.03/L$ $(0.37/L)$ resonant with the bulk (edge) mode, as shown in Fig. 3c (d), the light intensities $\left|a_{(r,u,l,d),nm}/A^{(0)}_\mathrm{in}\right|^2$ display that the light propagates in the bulk and along the boundary, respectively.

Non-linear regime.— The nonlinear Kerr medium with the self-focusing effect [35, 36] on the right hand side of three birefringent elements generates an attractive interaction $\chi < 0$ of photons with the same polarization. Here, we consider separately $\sigma_\pm$ polarizations found for the eigenmodes of the linear system, and thereby avoid the complexity of nonlinear birefringence for $\sigma_\pm$ polarizations propagating simultaneouly in the fiber links with χ [35, 37]. In the horizontal link between nodes (n, m) and $(n, m-1)$, light propagation in the Kerr medium is described by the right- and left- moving fields $\phi_{r,nm}(x,t)$ and $\phi_{l,nm-1}(x,t)$, which obey a set of nonlinear motion equations [38–40]. Similarly, the up- and down- moving fields $\phi_{u,nm}(x,t)$ and $\phi_{d,n+1m}(x,t)$ describe the light propagation in the vertical fiber connecting nodes (n, m) and $(n+1, m)$. Here, x is the coordinate along the fiber.

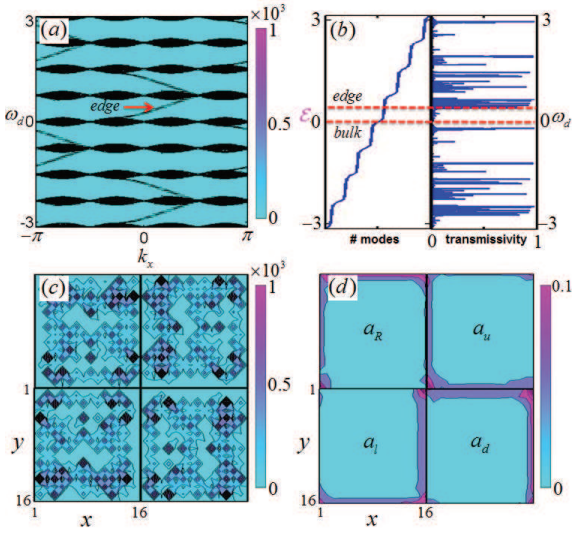

FIG. 3: (Color Online) Detection of topological properties, where $\theta_0 = \pi/2$, $r_\mathrm{BM} = 0.9$, and L is taken as unit. (a) For the cylindrical geometry, the contourplot of $d\Delta/d\omega_\mathrm{d}$ shows the eigen-spectrum for the network of size 48×48; (b) For the open plane of size 16×16, the eigen-spectrum for the closed network, and the transmission spectrum; (c)-(d): The light intensities $\left|a_{(r,u,l,d)}/A^{(0)}_\mathrm{in}\right|^2$ of (c) bulk and (d) edge modes in the network under σ_+-polarized driving light, where the first (second) row shows the right- (left-) and up- (down-) moving internal fields.

Under the circularly polarized driving field $A^{(0)}_{\mathrm{in},m}e^{-i\omega_\mathrm{d}t}$ with amplitude $A^{(0)}_{\mathrm{in},m} = A^{(0)}_\mathrm{in}e^{ik_x m}/\sqrt{N_x}$ through the top boundary of cylindrical network, the fields $\phi^{(0)}_{s,nm}(x,t) = \phi^{(0)}_{s,nm}(x)e^{-i\omega_\mathrm{d}t}$ $(s = r, u, l, d)$ in the steady state are plane waves $\phi^{(0)}_{r(u),nm}(x) = a_{r(u),nm}e^{ik_{r(u)}(x-L)}$, $\phi^{(0)}_{l,nm}(x) = e^{-in\sigma\theta_0}a_{l,nm}e^{-ik_l x}$, and $\phi^{(0)}_{d,nm}(x) = a_{d,nm}e^{-ik_d x}$, where $\omega_\mathrm{d} - k_s$ is determined by the elements of 4×4 diagonal matrices $\mathcal{N}_{nm}$ proportional to the light intensities $|a_{r,u,l,d}|^2$, and the amplitudes Ψ_{nm} in the bulk satisfy the non-linear scattering equation (Sec. III in [33])

$$S_0\Psi_{nm} = e^{-i\omega_\mathrm{d}L}e^{i\chi\mathcal{N}_{nm}L}\tilde{\Psi}_{nm}. \quad (1)$$

The light distribution in the network is characterized by Eq. (1) and the boundary conditions

$$b_{u,0m} = \frac{a_{d,1m}}{ir_\mathrm{BM}}e^{-i\omega_\mathrm{d}L} - \frac{t_\mathrm{BM}}{ir_\mathrm{BM}}A^{(0)}_{\mathrm{in},m}e^{-i\omega_\mathrm{d}L/2} \quad (2)$$

and $a_{d,N_y+1m} = a_{u,N_y m}$ on the top and bottom edges, respectively, where $b_{u,0m} = (ia_{r,1m} + a_{l,1m})/\sqrt{2}$ and $t_\mathrm{BM} = \sqrt{1 - r^2_\mathrm{BM}}$. The translational symmetry in Eq. (1) and boundary conditions give rise to $a_{(r,u,l,d),nm} = a_{(r,u,l,d),n}e^{ik_x m}/\sqrt{N_x}$.

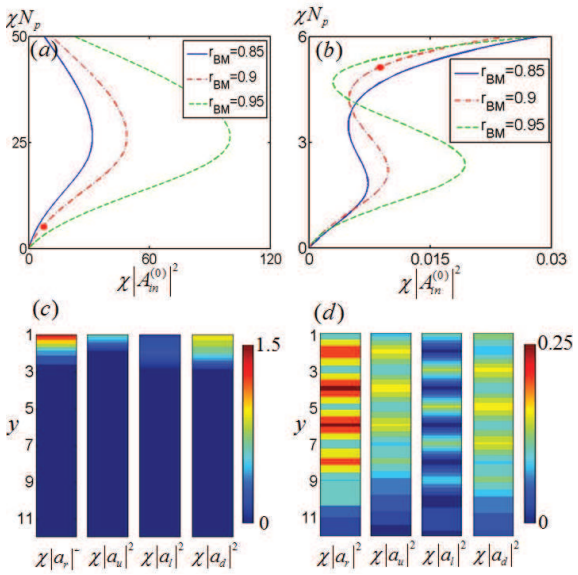

FIG. 4: (Color Online) Light distributions of the nonlinear system on the cylinder, where the size is 24×12, $\theta_0 = \pi/2$, $k_x = 0.26$, and L is taken as unit. The relation of the total intensity of (a) edge and (b) bulk modes in the network with different reflection indices $r_{\rm BM}$ and the input intensity of driving light with frequencies (a) $\omega_{\rm d}^{(1)} = 0.22$ and (b) $\omega_{\rm d}^{(2)} = 4.5 \times 10^{-2}$. The stable internal intensities of (c) edge and (d) bulk modes for $|\chi|\, N_{\rm p} = 5$ and $r_{\rm BM} = 0.9$ (the red dots).

By numerically solving Eq. (1), we show the total light intensity $N_{\rm p} = \sum_{n,s=r,u,l,d} |a_{s,n}|^2$ versus the driving strength $\left|A_{\rm in}^{(0)}\right|^2$ in the first row of Fig. 4 for $\omega_{\rm d}^{(1)} \sim 0.22/L$ (Fig. 4a) and $\omega_{\rm d}^{(2)} \sim 4.5 \times 10^{-2}/L$ (Fig. 4b), respectively, where $k_x \sim 0.26$ and the size of network is $N_x = 24$, $N_y = 12$. The $|\chi|\, N_{\rm p}$ versus $|\chi| \left|A_{\rm in}^{(0)}\right|^2$ curves display that for the given parameters (k_x,$\omega_{\rm d}$), the driving light with the amplitude $A_{\rm in}^{(0)}$ generates multiple light intensities in the steady state of the network [33]. As discussed in the following section (also Sec. IV in Ref. [33]), large domains of the steady state solutions in Fig. 4a and b are unstable to small perturbations. Here, we consider only stable solutions. The qualitative origin of these complex stabilities can be traced to the behavior of a single fiber segment with mirrors [33, 40].

For driving frequencies $\omega_{\rm d}^{(1)}$ and $\omega_{\rm d}^{(2)}$, Figs. 4c, d show that distinct light distribution $|\chi| \left|a_{(r,u,l,d),n}\right|^2$ are generated for interacting edge and bulk modes. Here, the total intensity $|\chi|\, N_{\rm p} = 5/L$ and $r_{\rm BM} = 0.9$. We emphasize that the topologically protected chiral edge mode survives even in the nonlinear regime, where the chirality is displayed by the dominating right-moving intensity in Fig. 4c.

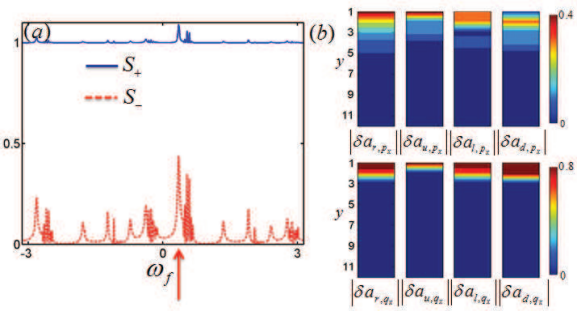

FIG. 5: (Color Online) Bogoliubov fluctuations on the cylinder, where the system size is 24×12, $\theta_0 = \pi/2$. The amplitude $|\delta A_{\rm in}^{(+)}|$ of the probe light and L are taken as unit. (a) The squeezing spectra of probe field with the positive frequency, where the Bogoliubov fluctuations above the stable edge steady states are generated; (b) The distributions of Bogoliubov edge fluctuations above the stable edge steady states, where the Bogoliubov excitation has the frequency $\omega_{\rm f} = 0.35$ as shown by the red arrow in (a).

Bogoliubov excitations in non-linear optics.— Additional weak probe light $\delta A_m^{\rm in}(t) = \sum_{\nu=\pm} \delta A_{{\rm in},m}^{(\nu)} e^{-i\nu\omega_{\rm f} t}$ through the top boundary induces the fluctuations

$$\delta\phi_{s,nm}(x,t) = \frac{1}{\sqrt{N_x}}[\delta\psi_{s,n,p_x}(x) e^{ip_x m} e^{-i\omega_{\rm f} t} + \delta\psi_{s,n,q_x}(x) e^{iq_x m} e^{i\omega_{\rm f} t}] \quad (3)$$

around steady states, where the reflected fluctuation field from the network is $\delta A_m^{\rm out}(t) = \sum_{\nu=\pm} \delta A_{{\rm out},m}^{(\nu)} e^{-i\nu\omega_{\rm f} t}$. Here, the positive- and negative- frequency ($\pm\omega_{\rm f}$) components $\delta A_{{\rm in(out)},m}^{(\pm)} = e^{ik_x m} \delta A_{\rm in(out)}^{(\pm)} e^{\pm i(p_x - k_x)m}/\sqrt{N_x}$ have the quasi-momenta p_x and $q_x = 2k_x - p_x$, respectively.

By linearization of nonlinear motion equations around the steady state in each fiber [38–40], the S-matrix of nodes and the boundary conditions of the cylindrical network result in the input-output relation $(\delta A_{\rm out}^{(+)}, \delta A_{\rm out}^{(-)*})^T = M_{\rm IO}(\delta A_{\rm in}^{(+)}, \delta A_{\rm in}^{(-)*})^T$ and the scattering equation (Sec. IV in [33])

$$\mathbf{D}(\omega_{\rm f}) \begin{pmatrix} \delta\mathbf{a}_{p_x} \\ \delta\mathbf{a}_{q_x}^* \end{pmatrix} = t_{\rm BM} \begin{pmatrix} \delta\mathbf{A}_{\rm in}^{(+)} e^{i(\omega_{\rm d} - \omega_{\rm f})\frac{L}{2}} \\ \delta\mathbf{A}_{\rm in}^{(-)*} e^{-i(\omega_{\rm d} + \omega_{\rm f})\frac{L}{2}} \end{pmatrix} \quad (4)$$

for the fluctuation fields $\delta\mathbf{a}_{p_x} = (\delta a_{r,n,p_x}, \delta a_{u,n,p_x}, \delta a_{l,n,p_x}, \delta a_{d,n,p_x})^T$ around the steady state configuration $a_{s,n}$. Here, $\delta\mathbf{A}_{\rm in}^{(\pm)} = \delta A_{\rm in}^{(\pm)}(\mathbf{0}, \mathbf{0}, \mathbf{0}, \mathbf{1})^T$ is composed of the null vector $\mathbf{0}$ and $\mathbf{1} = (1, 0, ..., 0)$, which are of dimension N_y. The steady-state is stable if all roots $\mathcal{E}_f$ of $\det\mathbf{D}(\omega_{\rm f})$ satisfy ${\rm Im}\mathcal{E}_f < 0$.

The stability of the solutions in Fig. 4 is analyzed by solving $\det\mathbf{D}(\mathcal{E}_f) = 0$, which shows that the steady states in Fig. 4c, d are stable. Induced by the "condensation" $a_{s,n}$ in the steady state, the fluctuation $\delta\mathbf{a}_{p_x}$

couples to the conjugate amplitude $\delta\mathbf{a}^*_{q_x}$, known as the Bogoliubov fluctuation. As a result, the probe light with positive frequency ($\delta A^{(-)}_{\rm in}=0$) and momentum p_x generates the Bogoliubov fluctuations (3) with frequencies $\pm\omega_{\rm f}$, which eventally gives rise to the emission of "classically" squeezed light $\delta A_{{\rm out},m}(t)$ [41]. The squeezing behavior is characterized by the squeezing spectra $S_+ = \left|\delta A^{(+)}_{\rm out}/\delta A^{(+)}_{\rm in}\right|$ and $S_- = \left|\delta A^{(-)}_{\rm out}/\delta A^{(+)}_{\rm in}\right|$ of reflected light, where $S_+^2 - S_-^2 = 1$ reflects the bosonic nature of light.

Around the stable edge steady state (Fig. 4c), the probe field with momentum $p_x \sim 0.52$ induces the generation of squeezed light with the spectra displayed in Fig. 5a. The peak around the frequency $\omega_{\rm f} \sim 0.35/L$ in the squeezing spectra is the signature of the Bogoliubov fluctuation $\delta\mathbf{a}_{p_x}$ and $\delta\mathbf{a}^*_{q_x}$ in the network. As shown in Fig. 5b, the large light distribution at the top boundary generates strong coupling of Bogoliubov fluctuations localized at the edge, which results in comparable magnitudes of $\delta\mathbf{a}_{p_x}$ and $\delta\mathbf{a}^*_{q_x}$.

In the bulk steady state (Fig. 4d), edge fluctuations can also be generated by the probe light with frequency $\omega_{\rm f} \sim 1.19/L$ and $p_x \sim 0.26$. However, in contrast to the Bogoliubov excitation in the edge steady state in Fig. 5, due to the small light distribution along the boundary, the counterpart $\left|\delta\mathbf{a}^*_{q_x}\right| \ll \left|\delta\mathbf{a}_{p_x}\right|$ of edge Bogoliubov fluctuations hardly response to the driving field with positive frequency (e.g. $\left|\delta\mathbf{a}^*_{q_x}/\delta A^{(+)}_{\rm in}\right| \sim 10^{-3}$).

Conclusions.— We propose to realize QSH effects of classical light with broad topological band gaps by optically passive elements in a 2D network. For the linear network, we find robust helical edge modes in broad topological band gaps, and investigate their generation and detection. In the nonlinear network, the interplay of the Kerr nonlinearities and topological effects gives rise to interacting edge (bulk) steady states and squeezed edge fluctuations around these steady states.

The work was funded by the European Union Integrated project SIQS. HJK acknowledges support as a Max Planck Institute for Quantum Optics Distinguished Scholar, as well as funding from NSF Grant PHY-1205729, the DOD NSSEFF program, the AFOSR QuMPASS MURI, the ONR QOMAND MURI, and the IQIM, an NSF Physics Frontiers Center with support of the Moore Foundation.

[1] D. J. Thouless, M. Kohmoto, M. P. Nightingale, and M. den Nijs, Phys. Rev. Lett. **49**, 405 (1982).
[2] F. D. M. Haldane, Phys. Rev. Lett. **61**, 2015 (1988).
[3] M. Z. Hasan and C. L. Kane, Rev. Mod. Phys. **82**, 3045 (2010).
[4] X.-L. Qi and S. C. Zhang, Rev. Mod. Phys. **83**, 1057 (2011).
[5] C. L. Kane and E. J. Mele, Phys. Rev. Lett. **95**, 226801 (2005).
[6] M. König, Science **318**, 766 (2007).
[7] D. Hsieh, D. Qian, L. Wray, Y. Xia, Y. S. Hor, R. J. Cava and M. Z. Hasan, Nature **452**, 970 (2008).
[8] H. Zhang, C. Liu, X. Qi, X. Dai, Z. Fang, and S. C. Zhang, Nat. Phys. **5**, 438 (2009).
[9] C. Z. Chang *et al.*, Science, **340**, 167 (2013).
[10] C. L. Kane and E. J. Mele, Phys. Rev. Lett. **95**, 146802 (2005).
[11] L. Fu and C. L. Kane, Phys. Rev. B, **74** 195312 (2006).
[12] X. G. Wen, Int. J. Mod. Phys. B **6**, 1711 (1992).
[13] R. B. Laughlin, Phys. Rev. Lett. **50**, 1395 (1983).
[14] G. Moore and N. Read, Nucl. Phys. B **360**, 362 (1991).
[15] M. Hafezi, S. Mittal, J. Fan, A. Migdall and J. M. Taylor, Nat. Photon. **7**, 1001 (2013).
[16] M. C. Rechtsman, J. M. Zeuner, Y. Plotnik, Y. Lumer, D. Podolsky, F. Dreisow, S. Nolte, M. Segev and A. Szameit, Nature **469**, 196 (2013).
[17] J. Dalibard, J. Gerbier, F. Juzeliūnas, and G. Öhberg, Rev. Mod. Phys. **83**, 1523 (2011).
[18] T. Shi and J. I. Cirac, Phys. Rev. A **87**, 013606 (2013).
[19] F. D. M. Haldane and S. Raghu, Phys. Rev. Lett. **100**, 013904 (2008).
[20] Z. Wang, Y. Chong, J. D. Joannopoulos, and M. Soljačić, Nature **461**, 772 (2009).
[21] K. Fang, Z. Yu, and S. Fan, Nat. Photon. **6**, 782 (2012).
[22] L. Yuan and S. Fan, Phys. Rev. A **92**, 053822 (2015).
[23] S. Walter and F. Marquardt, arXiv:1510.06754.
[24] V. Peano, M. Houde, C. Brendel, F. Marquardt, and A. A. Clerk, arXiv:1508.01383.
[25] R. O. Umucalılar and I. Carusotto, Phys. Rev. Lett. **108**, 206809 (2012).
[26] M. Hafezi, E. A. Demler, M. D. Lukin, and J. M. Taylor, Nat. Phys. **7**, 907 (2011).
[27] R. O. Umucalılar and I. Carusotto, Phys. Rev. A **84**, 043804 (2011).
[28] A. B. Khanikaev, S. H. Mousavi,W. K. Tse, M. Kargarian, A. H. MacDonald, and G. Shvets, Nat. Mater. **12**, 233 (2013).
[29] J. B. Pendry, A. J. Holden, W. J. Stewart and I. Youngs, Phys. Rev. Lett. **76**, 4773 (1996).
[30] D. R. Smith, W. J. Padilla, D. C. Vier, S. C. Nemat-Nasser, and S. Schultz, Phys. Rev. Lett. **84**, 4184 (2000).
[31] O. Bahat-Treidel and M. Segev, Phys. Rev. A **84**, 021802(R) (2011).
[32] R. Bekenstein, J. Nemirovsky, I. Kaminer, and M. Segev, Phys. Rev. X **4**, 011038 (2014).
[33] See the supplemental material accompanying this paper, where we explain the constructions at nodes and in fibers, derive the scattering equations for steady states of the light propagating in the single fiber and the whole network, and analyze the steady-state stability by investigating the behaviors of Bogoliubov fluctuations.
[34] D. R. Hofstadter, Phys. Rev. B **14**, 2239 (1976).
[35] G. P. Agrawal, *Nonlinear Fiber Optics*, Academic Press, 2013.
[36] R. Adair, L. L. Chase, and S. A. Payne, Phys. Rev. B **39**,3337 (1989).
[37] R. W. Boyd, *Nonlinear Optics*, Academic Press, 2008.
[38] M. Yu, C. J. McKinstrie, and G. P. Agrawal, J. Opt. Soc. Am. B **15**, 607 (1998).
[39] M. Yu, C. J. McKinstrie, and G. P. Agrawal, J. Opt. Soc.

Am. B **15**, 627 (1998).
[40] W.J. Firth, Opt. Commun. **39**, 343 (1981).
[41] We emphasize that our results from the fluctuation analysis for the classical light are also valid in the quantum regime, where the squeezing behaviors of quantum edge fluctuations arise from the interplay of the Kerr nonlinearities and topological effects.

Supplemental Material

This supplemental material is divided in four sections. In the first one, Sec. SMI, we explain the construction of nodes, where two beamsplitters and two perfect mirrors are applied to change the propagation directions of the light in fibers. The analytical expression for the S-matrix for each node is given explicitly.

The second section (Sec. SMII) is devoted to analyze the light propagation in the fiber as a Kerr medium. After solving the nonlinear equations that describe the light propagating in the horizontal and vertical fibers, in Sec. SMIIA we investigate the properties of Bogoliubov fluctuations by linearizing the nonlinear equations around the steady state solutions. To get insight into the steady-state stability of the whole network, in Sec. SMIIB we utilize a single nonlinear Fabry-Perot cavity as an paradigmatic example to analyze the stability of steady states.

By combining the results of S-matrices at each node (Sec. SMI) and in fibers (Sec. SMIIA), in Sec. SMIII we derive a nonlinear scattering equation in the whole network with different geometries, which determines the steady state properties. The dynamics of fluctuations in each fiber obey the linearized Bogoliubov equation (Sec. SMIIA), together with the S-matrix of nodes, which results in a linear scattering equation of Bogoliubov fluctuations in the network. The linear scattering equation is used to analyze the stability of steady states in the network.

SMI-CONSTRUCTION OF NODES

In this section, we show the construction of the node by two beamsplitters and two perfect mirrors, and derive the S-matrix of the node. Since the polarizations of light are always orthogonal to the propagation direction, the directions of vertical polarizations are different in the horizontal and vertical fibers. As shown in Fig. SM1a, the horizontal polarizations in the fibers are chosen to be pointing out of the 2D plane, while the vertical polarizations are pointing up and right in the horizontal and vertical fibers, respectively.

As shown in Fig. SM1a, the input and output amplitudes of the node are $a_{r,u,l,d}$ and $b_{r,u,l,d}$, respectively. The input and output amplitudes of the beamsplitter A in the inner-cavity are $c_{u,l}$ and $c_{r,d}$, respectively. Elements C and D are perfectly reflecting mirrors. For the beamsplitters A, B, the amplitudes obey the scattering equations

$$S_{\rm bs}^{(A)}\begin{pmatrix}\sigma_z a_r\\ c_u\\ c_l\\ a_d\end{pmatrix}=\begin{pmatrix}c_r\\ b_u\\ \sigma_z b_l\\ c_d\end{pmatrix};S_{\rm bs}^{(B)}\begin{pmatrix}c_d\\ \sigma_z a_u\\ a_l\\ c_r\end{pmatrix}=\begin{pmatrix}b_r\\ c_l\\ c_u\\ \sigma_z b_d\end{pmatrix}, \tag{SM1}$$

where we assume that the size of the node is much smaller than the wavelength of light such that the free propagation phase in the node can be neglected, and the two-component amplitudes $a_{r,u,l,d}$, $b_{r,u,l,d}$, and $c_{r,u,l,d}$ are defined in the polarization basis (H,V). The Jones matrix σ_z is introduced to describe the two birefringent elements (E,F) in close proximity to the beamsplitters (A,B). The S-matrix $S_{\rm bs}^{(A)}=S_{\rm bs}^{(B)}=S_{\rm bs}$:

$$S_{\rm bs}=\begin{pmatrix}t_{\rm bs} & ir_{\rm bs}\sigma_z & 0 & 0\\ ir_{\rm bs}\sigma_z & t_{\rm bs} & 0 & 0\\ 0 & 0 & t_{\rm bs} & ir_{\rm bs}\sigma_z\\ 0 & 0 & ir_{\rm bs}\sigma_z & t_{\rm bs}\end{pmatrix} \tag{SM2}$$

for the beamsplitter is given by the real reflection and transmission coefficients $r_{\rm bs}$ and $t_{\rm bs}=\sqrt{1-r_{\rm bs}^2}$, where the matrix σ_z describes the direction change of the vertical polarization due to the Fresnel reflection rule.

By elimination of the fields in the ring cavity formed by elements A, B, C, D and by incorporating the elements (E,F), we establish the scattering equation for the node $S_{\rm node}\Psi_a=\Psi_b$, where the S-matrix

$$S_{\rm node}=\begin{pmatrix}0 & ir_{\rm node} & 0 & t_{\rm node}\\ ir_{\rm node} & 0 & t_{\rm node} & 0\\ 0 & t_{\rm node} & 0 & ir_{\rm node}\\ t_{\rm node} & 0 & ir_{\rm node} & 0\end{pmatrix} \tag{SM3}$$

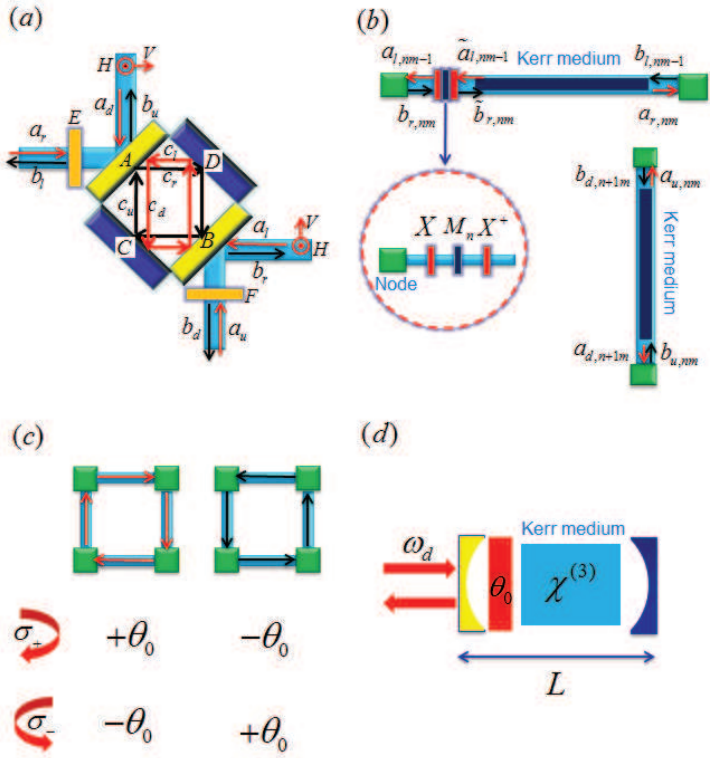

FIG. SM1: (Color Online) Schematic for the nodes, the horizontal and vertical fibers, the plaquette in the network, and a single Fabry-Perot cavity: (a) A node connects horizontal and vertical links. Here, $a_{r,u,l,d}$ and $b_{r,u,l,d}$ denote the input and output amplitudes, and $c_{r,u,l,d}$ denote the amplitudes in the cavity. The horizontal and vertical polarizations (H,V) in fibers are shown by the red dots and arrows. (b) The horizontal and the vertical links with the Kerr medium and birefringent elements, where the Kerr medium is put on the right hand side of three birefringent elements in the horizontal link, where the birefringent elements are assumed to have no Kerr nonlinearity ($\chi = 0$). From left to right, the three birefringent elements are described by the Jones matrices $X = e^{i\pi\sigma_x/4}$, $M_n = e^{in\theta_0\sigma_z}$, and $X^\dagger$ in the linear polarization basis (H,V). (c) The σ_+ polarized light acquires the phase θ_0 ($-\theta_0$) by propagating (anti-) clockwisely in each plaquette, while the σ_- polarized light acquires the phase $-\theta_0$ (θ_0) by propagating (anti-) clockwisely in each plaquette. (d) A single Fabry-Perot cavity with Kerr nonlinearity and an anisotropic phase plate placed next to the left end-mirror to mimic the horizontal link, where the driving field with frequency ω_d is applied.

relates the input amplitudes $\Psi_a = (a_r, a_u, a_l, a_d)^T$ and the output amplitudes $\Psi_b = (b_r, b_u, b_l, b_d)^T$. The effective reflection and transmission coefficients of the node are $r_{\rm node} = 2r_{\rm bs}/(1+r_{\rm bs}^2)$ and $t_{\rm node} = t_{\rm bs}^2/(1+r_{\rm bs}^2)$. In our scheme, $r_{\rm node} = t_{\rm node} = 1/\sqrt{2}$ and the corresponding reflection coefficient of the node is $r_{\rm bs} = \sqrt{2}-1$.

SMII-LIGHT PROPAGATION IN FIBERS

This section is divided in two subsections. In Sec. SMIIA, the propagation of the light in a fiber with the non-linear Kerr medium is analyzed. In Sec. SMIIB, a simple nonlinear system, i.e., a single Fabry-Perot cavity, is analyzed, where the stability of steady states is investigated.

SMIIA-Steady-state solutions and fluctuations in fibers

As shown in Fig. SM1b, without loss of generality, the three birefringent elements are placed close to the node on the left side of the horizontal fiber, and the Kerr medium is on the right hand side of these birefringent elements. The oppositely directed effective magnetic fields for circular polarized light $\sigma_\pm$ are generated by the birefringences, as shown in Fig. SM1c.

As shown by Eq. (SM37) in Sec. SMIII, two $\sigma_\pm$ polarized light are decoupled in the linear network. Hence, in the analysis of nonlinear system, we are able to treat the $\sigma_\pm$ polarizations independently, as long as these polarizations are separately excited by the external input (i.e., only σ_+ OR σ_- polarization circulating in the fiber links). Alternatively, by fiat we set to zero terms related to cross phase modulation between orthogonal circular polarizations in this first analysis of the nonlinear system, as discussed in Chapter 6 of Ref. [35] and Chapter 4 of Ref. [37].

In the Kerr medium of the fiber connecting nodes (n,m) and $(n,m-1)$, the right- and left- moving fields obey the motion equations [38–40]

$$\begin{aligned} & i\partial_t\phi_{r,nm}(x,t)+i\partial_x\phi_{r,nm}(x,t) \\ = \;& \chi[|\phi_{r,nm}(x,t)|^2+2\,|\phi_{l,nm-1}(x,t)|^2]\phi_{r,nm}(x,t), \end{aligned} \tag{SM4}$$

and

$$\begin{aligned} & i\partial_t\phi_{l,nm-1}(x,t)-i\partial_x\phi_{l,nm-1}(x,t) \\ = \;& \chi[|\phi_{l,nm-1}(x,t)|^2+2\,|\phi_{r,nm}(x,t)|^2]\phi_{l,nm-1}(x,t), \end{aligned} \tag{SM5}$$

where x is the distance along the fiber and the cross Kerr interaction of fields with orthogonal polarizations is neglected.

The formal solutions for Eqs. (SM4) and (SM5) are

$$\begin{aligned} \phi_{r,nm}(x,t) &= [a_{r,nm}+\delta\phi_{r,nm}(x,t)]e^{ik_r(x-L)}e^{-i\omega t}, \\ \phi_{l,nm-1}(x,t) &= [\tilde{a}_{l,nm-1}+\delta\phi_{l,nm-1}(x,t)]e^{-ik_l x}e^{-i\omega t}, \end{aligned} \tag{SM6}$$

where $\delta\phi_{r,nm}$ and $\delta\phi_{l,nm-1}$ are the fluctuations around the steady state solutions $a_{r,nm}$ and $\tilde{a}_{l,nm-1}$. As shown in Fig. SM1b, $a_{r,nm}$ is the amplitude of the right-moving input field to the node (n,m), and $\tilde{a}_{l,nm-1}$ is the amplitude of the left-moving input field to birefringent elements. The wave vectors

$$\begin{aligned} k_r &= \omega-\chi[|a_{r,nm}|^2+2\,|\tilde{a}_{l,nm-1}|^2], \\ k_l &= \omega-\chi[|\tilde{a}_{l,nm-1}|^2+2\,|a_{r,nm}|^2], \end{aligned} \tag{SM7}$$

of the right- and left-moving fields are given by the intensities of the fields and the characteristic frequency ω, where $\omega=\mathcal{E}$ is the eigenfrequency of the closed network, and $\omega=\omega_{\rm d}$ is the frequency of the driving field applied to the open network.

The steady state solution establishes the relations

$$\begin{aligned} e^{-in\sigma\theta_0}b_{r,nm} &= \tilde{b}_{r,nm}=e^{-ik_rL}a_{r,nm}, \\ e^{in\sigma\theta_0}b_{l,nm-1} &= e^{-ik_lL}e^{in\sigma\theta_0}\tilde{a}_{l,nm-1}=e^{-ik_lL}a_{l,nm-1}, \end{aligned} \tag{SM8}$$

where, as shown in Fig. SM1b, $b_{r,nm}$ is the amplitude of the right-moving output field from the node $(n,m-1)$, $\tilde{b}_{r,nm}$ is the amplitude of the right-moving on the right hand side of birefringent elements, $b_{l,nm-1}$ is the amplitude of the left-moving output field from the node (n,m), $a_{l,nm-1}$ is the amplitude of the left-moving input field to the node $(n,m-1)$, and $\sigma=\pm1$ denotes the two orthogonal circular polarizations.

Around the steady state solution, the motion equations (SM4) and (SM5) are linearized as

$$i\partial_t\delta\Psi+\mathbf{\Sigma}\partial_x\delta\Psi=\mathbf{M}_H\delta\Psi \tag{SM9}$$

for the Bogoliubov fluctuation $\delta\Psi=(\delta\phi_{r,nm},\delta\phi_{l,nm-1},\delta\phi^*_{r,nm},\delta\phi^*_{l,nm-1})^T$, where the matrices are

$$\mathbf{\Sigma}=i\begin{pmatrix}1&0&0&0\\0&-1&0&0\\0&0&1&0\\0&0&0&-1\end{pmatrix}, \tag{SM10}$$

and

$$\mathbf{M}_H{=}\chi\begin{pmatrix}|a_{r,nm}|^2 & 2\tilde{a}^*_{l,nm-1}a_{r,nm} & a^2_{r,nm} & 2a_{r,nm}\tilde{a}_{l,nm-1}\\ 2a^*_{r,nm}\tilde{a}_{l,nm-1} & |\tilde{a}_{l,nm-1}|^2 & 2a_{r,nm}\tilde{a}_{l,nm-1} & \tilde{a}^2_{l,nm-1}\\ -a^{*2}_{r,nm} & -2a^*_{r,nm}\tilde{a}^*_{l,nm-1} & -|a_{r,nm}|^2 & -2a^*_{r,nm}\tilde{a}_{l,nm-1}\\ -2a^*_{r,nm}\tilde{a}^*_{l,nm-1} & -\tilde{a}^{*2}_{l,nm-1} & -2\tilde{a}^*_{l,nm-1}a_{r,nm} & -|\tilde{a}_{l,nm-1}|^2\end{pmatrix}. \tag{SM11}$$

The Bogoliubov mode $\delta\Psi = \delta\psi e^{-i\omega_{\rm f}t}$ with the fluctuation frequency $\omega_{\rm f}$ around ω obeys the equation

$$\omega_{\rm f}\delta\psi + \mathbf{\Sigma}\partial_x\delta\psi = \mathbf{M}_H\delta\psi, \tag{SM12}$$

where the time-independent field $\delta\psi = (\delta\psi_{r,nm}, \delta\psi_{l,nm-1}, \delta\psi^*_{r,nm}, \delta\psi^*_{l,nm-1})^T$.

The formal solution of Eq. (SM12) leads to the relation

$$e^{\mathbf{\Sigma}(\omega_{\rm f}-\mathbf{M}_H)L}\begin{pmatrix} e^{-in\sigma\theta_0}\delta b_{r,nm} \\ e^{-in\sigma\theta_0}\delta a_{l,nm-1} \\ e^{in\sigma\theta_0}\delta b^*_{r,nm} \\ e^{in\sigma\theta_0}\delta a^*_{l,nm-1}\end{pmatrix} = \begin{pmatrix} \delta a_{r,nm} \\ \delta b_{l,nm-1} \\ \delta a^*_{r,nm} \\ \delta b^*_{l,nm-1}\end{pmatrix} \tag{SM13}$$

of the input and output fluctuation fields

$$\delta a_{r,nm} = \delta\psi_{r,nm}(L), \delta a_{l,nm-1} = e^{in\sigma\theta_0}\delta\psi_{l,nm-1}(0), \tag{SM14}$$

and

$$\delta b_{r,nm} = e^{in\sigma\theta_0}\delta\psi_{r,nm}(0), \delta b_{l,nm-1} = \delta\psi_{l,nm-1}(L), \tag{SM15}$$

around the steady state amplitudes $a_{r,nm}$ ($\delta a_{l,nm-1}$) and $b_{r,nm}$ ($b_{l,nm-1}$).

The same analysis is applied to light propagation in the vertical fiber connecting nodes (n,m) and $(n+1,m)$. The relations for the amplitudes of the input fields $a_{u,nm}, a_{d,n+1m}$ and the output field $b_{u,nm}, b_{d,n+1m}$ (as shown in Fig. SM1b) in the steady state are

$$b_{u,nm} = e^{-ik_uL}a_{u,nm}, b_{d,n+1m} = e^{-ik_dL}a_{d,n+1m}, \tag{SM16}$$

where the wavevectors are

$$\begin{aligned} k_u &= \omega - \chi[|a_{u,nm}|^2 + 2\,|a_{d,n+1m}|^2], \\ k_d &= \omega - \chi[|a_{d,n+1m}|^2 + 2\,|a_{u,nm}|^2]. \end{aligned} \tag{SM17}$$

The relation

$$e^{\mathbf{\Sigma}(\omega_{\rm f}-\mathbf{M}_V)L}\begin{pmatrix} \delta b_{u,nm} \\ \delta a_{d,n+1m} \\ \delta b^*_{u,nm} \\ \delta a^*_{d,n+1m}\end{pmatrix} = \begin{pmatrix} \delta a_{u,nm} \\ \delta b_{d,n+1m} \\ \delta a^*_{u,nm} \\ \delta b^*_{d,n+1m}\end{pmatrix} \tag{SM18}$$

relates the input and output fluctuation fields $\delta a_{u,nm}$ ($\delta a_{d,n+1m}$) and $\delta b_{u,nm}$ ($\delta b_{d,n+1m}$) around the steady state amplitudes $a_{u,nm}$ ($a_{d,n+1m}$) and $b_{u,nm}$ ($b_{d,n+1m}$), where

$$\mathbf{M}_V = \chi\begin{pmatrix} |a_{u,nm}|^2 & 2a^*_{d,n+1m}a_{u,nm} & a^2_{u,nm} & 2a_{u,nm}a_{d,n+1m} \\ 2a^*_{u,nm}a_{d,n+1m} & |a_{d,n+1m}|^2 & 2a_{u,nm}a_{d,n+1m} & a^2_{d,n+1m} \\ -a^{*2}_{u,nm} & -2a^*_{u,nm}a^*_{d,n+1m} & -|a_{u,nm}|^2 & -2a^*_{u,nm}a_{d,n+1m} \\ -2a^*_{u,nm}a^*_{d,n+1m} & -a^{*2}_{d,n+1m} & -2a^*_{d,n+1m}a_{u,nm} & -|a_{d,n+1m}|^2 \end{pmatrix}. \tag{SM19}$$

SMIIB-Nonlinear Fabry-Perot cavity

Before studying the steady state properties and the stability of the light in the whole network, we use a paradigmatic example, i.e., the single Fabry-Perot cavity with nonlinear Kerr medium [40] to show the stability analysis of steady states. Our goal is to understand better the stability analysis for more complex 2D arrays of nonlinear fibers and beam splitters.

As shown in Fig. SM1d, the cavity with a perfect right end-mirror is driven by the light with frequency $\omega_{\rm d}$ through a partially transmissive mirror at the left end. In the cavity, the phase plate is placed next to the transmissive mirror. In propagation from left to right, the light acquires the phase factor $e^{-i\theta_0}$. Here, $\theta_0 \neq 0$ ($\theta_0 = 0$) corresponds to the single horizontal (vertical) fiber in the network.

The relations

$$e^{-i\theta_0}b_r = e^{-ik_rL}a_r, e^{i\theta_0}b_l = e^{-ik_lL}a_l \tag{SM20}$$

of input a_r (a_l) and output amplitude b_r (b_l) follow from Eq. (SM8), where L is the cavity length, and

$$\begin{aligned} k_r &= \omega_{\rm d} - \chi(|a_r|^2 + 2|a_l|^2), \\ k_l &= \omega_{\rm d} - \chi(|a_l|^2 + 2|a_r|^2). \end{aligned} \tag{SM21}$$

At the end-mirrors, the boundary conditions are $a_r = b_l$, and

$$\begin{pmatrix} b_r \\ A^{(0)}_{\rm out} \end{pmatrix} = \begin{pmatrix} t_{\rm BM} & ir_{\rm BM} \\ ir_{\rm BM} & t_{\rm BM} \end{pmatrix} \begin{pmatrix} A^{(0)}_{\rm in} \\ a_l \end{pmatrix}, \tag{SM22}$$

where $t_{\rm BM}$ ($r_{\rm BM}$) is the real transmission (reflection) coefficients of the left end-mirror, and $A^{(0)}_{\rm in}$ ($A^{(0)}_{\rm out}$) is the input (output) amplitude of the cavity.

By eliminating the output amplitude b_r (b_l) in Eqs. (SM20) and (SM22), we obtain the nonlinear equation

$$a_r = \frac{t_{\rm BM}A^{(0)}_{\rm in}e^{-i\theta_0}}{e^{-ikL} - ir_{\rm BM}e^{ikL}}, \tag{SM23}$$

that determines the amplitude $a_r = |a_r|\, e^{i\theta_r}$, where $k_r = k_l \equiv k = \omega_{\rm d} - 3\chi|a_r|^2$, and the output amplitude

$$A^{(0)}_{\rm out} = ir_{\rm BM}A^{(0)}_{\rm in} + t_{\rm BM}a_l = \frac{e^{ikL} + ir_{\rm BM}e^{-ikL}}{e^{-ikL} - ir_{\rm BM}e^{ikL}}A^{(0)}_{\rm in} \tag{SM24}$$

of the cavity is determined by the relation $a_l = e^{i\theta_0}e^{ikL}a_r$. In the good cavity limit $t_{\rm BM} \to 0$, Eq. (SM23) determines the intensity-dependent frequency

$$\mathcal{E}_n = \frac{n\pi}{L} - \frac{\pi}{4L} + 3\chi|a_r|^2 \tag{SM25}$$

of the closed cavity, where n is an integer.

For different driving frequency $\omega_{\rm d}$, the relation

$$x = \frac{y}{1 - r^2_{\rm BM}}[1 + r^2_{\rm BM} + 2r_{\rm BM}\sin(2\omega_{\rm d}L - 6y)] \tag{SM26}$$

of $y = \chi|a_r|^2$ and the input intensity $x = \chi\left|A^{(0)}_{\rm in}\right|^2$ is shown in Fig. SM2a and SM2b, where $L = 1$ is taken as unit and $r_{\rm BM} = 0.85, 0.9, 0.95$. When the driving frequency $\omega_{\rm d}$ is resonant with the intrinsic frequency $\mathcal{E}_n$ of the closed cavity, the output field $A^{(0)}_{\rm out} = -iA^{(0)}_{\rm in}$.

The figures SM2a and SM2b show that for a given $\omega_{\rm d}$, the driving field with a fixed intensity $\left|A^{(0)}_{\rm in}\right|^2$ can generate multiple intracavity intensities. In order to analyze the stability of these multiple steady states, we investigate the energy spectrum of Bogoliubov fluctuations. It follows from Eq. (SM13) that the fluctuation fields satisfy

$$e^{\mathbf{\Sigma}(\omega_{\rm f} - U_{\rm s}^\dagger \mathbf{M}_{\rm s} U_{\rm s})L} \begin{pmatrix} e^{-i\theta_0}\delta b_r \\ e^{-i\theta_0}\delta a_l \\ e^{i\theta_0}\delta b^*_r \\ e^{i\theta_0}\delta a^*_l \end{pmatrix} = \begin{pmatrix} \delta a_r \\ \delta b_l \\ \delta a^*_r \\ \delta b^*_l \end{pmatrix}, \tag{SM27}$$

where the matrix

$$\mathbf{M}_{\rm s} = \chi|a_r|^2 \begin{pmatrix} 1 & 2e^{-ikL} & 1 & 2e^{ikL} \\ 2e^{ikL} & 1 & 2e^{ikL} & e^{2ikL} \\ -1 & -2e^{-ikL} & -1 & -2e^{ikL} \\ -2e^{-ikL} & -e^{-2ikL} & -2e^{-ikL} & -1 \end{pmatrix} \tag{SM28}$$

for the single fiber, and the unitary matrix $U_{\rm s} = I_2 \oplus e^{2i\theta_r}I_2$ is determined by the two-dimensional identity matrix I_2.

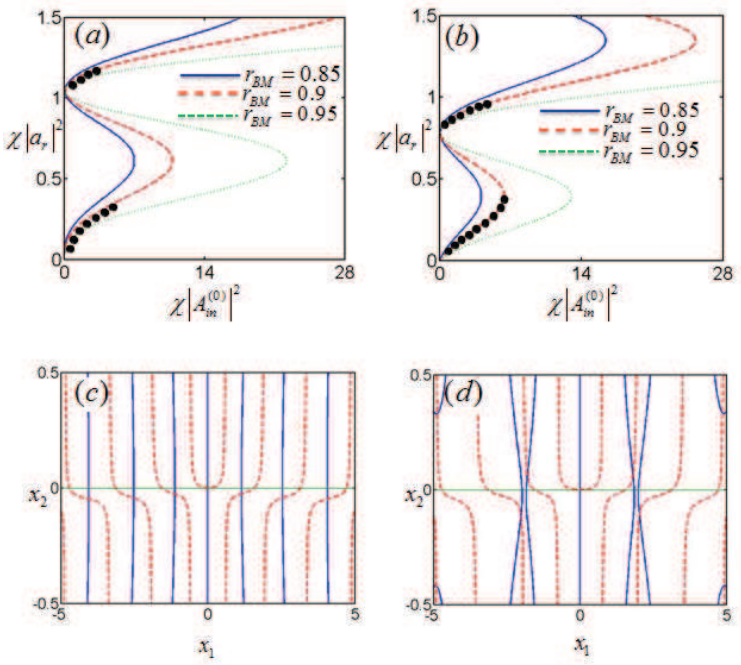

FIG. SM2: (Color Online) Steady state solutions and stability analysis, where L is taken as unit. (a)-(b): The relation of the light intensity $\chi|a_r|^2$ in the cavity and the driving field intensity $\chi\left|A_{\rm in}^{(0)}\right|^2$ in steady state for the driving frequencies $\omega_d=3\pi/4$ (a) and $\omega_d=\pi/2$ (b). Here, the stable regimes are marked by the black dots. (c)-(d): For $\omega_d=3\pi/4$, the first and second equations in (SM35) are shown by the solid (blue) and dashed (red) curves, where $\chi|A_{\rm in}|^2=1$, $\chi|a_r|^2=1.12$ (c) and $\chi|A_{\rm in}|^2=5$, $\chi|a_r|^2=1.21$ (d).

The fluctuation equation (SM27) leads to the relation $\delta\mathbf{B}=\tilde{U}_\theta U_b^{-1}U_aU_\theta\delta\mathbf{A}$ of $\delta\mathbf{B}=(\delta b_r,\delta b_l,\delta b_r^*,\delta b_l^*)^T$ and $\delta\mathbf{A}=(\delta a_r,\delta a_l,\delta a_r^*,\delta a_l^*)^T$, where the matrices

$$U_b=\begin{pmatrix} P_{\rm s,11} & 0 & P_{\rm s,13} & 0\\ -P_{\rm s,21} & 1 & -P_{\rm s,23} & 0\\ P_{\rm s,31} & 0 & P_{\rm s,33} & 0\\ -P_{\rm s,41} & 0 & -P_{\rm s,43} & 1\end{pmatrix},U_a=\begin{pmatrix} 1 & -P_{\rm s,12} & 0 & -P_{\rm s,14}\\ 0 & P_{\rm s,22} & 0 & P_{\rm s,24}\\ 0 & -P_{\rm s,32} & 1 & -P_{\rm s,34}\\ 0 & P_{\rm s,42} & 0 & P_{\rm s,44}\end{pmatrix} \tag{SM29}$$

are determined by the propagating matrix $P_{\rm s}=e^{\mathbf{\Sigma}(\omega_{\rm f}-U_{\rm s}^\dagger\mathbf{M}_{\rm s}U_{\rm s})L}$, and the diagonal matrices

$$U_\theta=\begin{pmatrix} 1 & 0 & 0 & 0\\ 0 & e^{-i\theta_0} & 0 & 0\\ 0 & 0 & 1 & 0\\ 0 & 0 & 0 & e^{i\theta_0}\end{pmatrix},\tilde{U}_\theta=\begin{pmatrix} e^{i\theta_0} & 0 & 0 & 0\\ 0 & 1 & 0 & 0\\ 0 & 0 & e^{-i\theta_0} & 0\\ 0 & 0 & 0 & 1\end{pmatrix}. \tag{SM30}$$

On the other hand, the boundary conditions at the end mirrors are $\delta a_r=\delta b_l e^{-ikL}$ and

$$\begin{pmatrix}\delta b_r e^{-ikL}\\ \delta A_{\rm out}\end{pmatrix}=\begin{pmatrix} t_{\rm BM} & ir_{\rm BM}\\ ir_{\rm BM} & t_{\rm BM}\end{pmatrix}\begin{pmatrix}\delta A_{\rm in}\\ \delta a_l\end{pmatrix}. \tag{SM31}$$

By eliminating the fluctuation field δB, we obtain the scattering equation

$$(\tilde{U}_\theta U_b^{-1}U_aU_\theta-U_kR_{\rm BM})\delta\mathbf{A}=t_{\rm BM}U_k\delta\mathbf{A}_d \tag{SM32}$$

with the driving term $\delta\mathbf{A}_d=(\delta A_{\rm in},0,\delta A_{\rm in}^*,0)^T$, where the matrices $U_k=e^{ikL}I_2\oplus e^{-ikL}I_2$ and

$$R_{\rm BM}=\begin{pmatrix} 0 & ir_{\rm BM} & 0 & 0\\ 1 & 0 & 0 & 0\\ 0 & 0 & 0 & -ir_{\rm BM}\\ 0 & 0 & 1 & 0\end{pmatrix}. \tag{SM33}$$

The zeros $D(\mathcal{E}_{\rm f})=0$ of the determinant

$$D(\omega_{\rm f})=\det(\tilde{U}_\theta U_b^{-1}U_aU_\theta-U_kR_{\rm BM}) \tag{SM34}$$

determines the stability of the steady state solution, where the steady state is stable if all $\mathrm{Im}\mathcal{E}_{\rm f}<0$.

For the good cavity limit $t_{\rm BM}\to 0$, the momentum $kL=n\pi-\pi/4$, and the eigenfrequency of Bogoliubov fluctuations is $\mathcal{E}_{\rm f}=n_{\rm f}\pi$, where $n_{\rm f}$ is an integer. For the open cavity, the condition $D(\mathcal{E}_{\rm f})=0$ leads to the two transcendental equations

$$\begin{aligned}\mathrm{Re}D(x_1+ix_2) &= 0,\\ \mathrm{Im}D(x_1+ix_2) &= 0,\end{aligned} \tag{SM35}$$

for $x_1=\mathrm{Re}\mathcal{E}_{\rm f}$ and $x_2=\mathrm{Im}\mathcal{E}_{\rm f}$. In Figs. SM2c and SM2d, we show the two curves given by Eq. (SM35) for different driving intensities $\chi\left|A_{\rm in}^{(0)}\right|^2$, where the intersections of two curves determines the solution x_1 and x_2. As shown in Fig. SM2d, the positive coordinates $x_2>0$ at points of intersection imply an unstable steady state. In Figs. SM2a and SM2b, the stable regimes are marked by the black dots, where these stable solutions are in the positive slope regimes of $\chi\left|a_r\right|^2$ versus $\chi\left|A_{\rm in}^{(0)}\right|^2$ curves.

SMIII-SCATTERING EQUATIONS ON DIFFERENT GEOMETRIES

In this section, we use the results (SM8) and (SM16) to derive the scattering equation for the amplitude $a_{r,u,l,d}$ in the steady state of the whole network. Here, in terms of different boundary conditions, we analyze the scattering equations describing the closed and open networks on the torus, cylindrical, and planar geometries.

The combination of Eqs. (SM8), (SM16) and the S-matrix $S_{\rm node}$ leads to the scattering equation

$$S_0\begin{pmatrix}a_{r,nm}\\ a_{u,nm}\\ a_{l,nm}\\ a_{d,nm}\end{pmatrix}=e^{-i\omega L}e^{i\chi\mathcal{N}_{nm}L}\begin{pmatrix}a_{r,nm+1}\\ a_{u,n-1m}\\ a_{l,nm-1}\\ a_{d,n+1m}\end{pmatrix} \tag{SM36}$$

for the input amplitudes of nodes in the bulk, where the S-matrix

$$S_0=\frac{1}{\sqrt{2}}\begin{pmatrix}0 & ie^{-in\sigma\theta_0} & 0 & e^{-in\sigma\theta_0}\\ i & 0 & 1 & 0\\ 0 & e^{in\sigma\theta_0} & 0 & ie^{in\sigma\theta_0}\\ 1 & 0 & i & 0\end{pmatrix} \tag{SM37}$$

describes the free propagation in the linear network, and the additional phase induced by the Kerr nonlinearity is depicted by the intensity matrix

$$\mathcal{N}_{nm}=\begin{pmatrix}\left|a_{r,nm+1}\right|^2+2\left|a_{l,nm}\right|^2 & 0 & 0 & 0\\ 0 & \left|a_{u,n-1m}\right|^2+2\left|a_{d,nm}\right|^2 & 0 & 0\\ 0 & 0 & \left|a_{l,nm-1}\right|^2+2\left|a_{r,nm}\right|^2 & 0\\ 0 & 0 & 0 & \left|a_{d,n+1m}\right|^2+2\left|a_{u,nm}\right|^2\end{pmatrix}. \tag{SM38}$$

Without the Kerr nonlinearity, i.e., $\chi=0$, the scattering matrix (SM37) shows that the $\sigma_\pm$ polarizations are decoupled.

SMIIIA-Closed network

For the network on the torus, the boundary condition is

$$\begin{aligned}a_{r,nN_x+1} &= a_{r,n1}, a_{l,n0}=a_{l,nN_x},\\ a_{u,0m} &= a_{u,N_ym}, a_{d,N_y+1m}=a_{d,1m},\end{aligned} \tag{SM39}$$

where the size of the network is $N_x \times N_y$. For the network on cylinder with the periodic boundary condition along x-direction,

$$\begin{aligned} a_{r,nN_x+1} &= a_{r,n1}, a_{l,n0} = a_{l,nN_x}, \\ a_{u,0m} &= a_{d,1m}, a_{d,N_y+1m} = a_{u,N_ym}. \end{aligned} \tag{SM40}$$

For the planar network with boundary mirrors of unit reflectivity, the boundary condition is

$$\begin{aligned} a_{r,nN_x+1} &= a_{l,nN_x}, a_{l,n0} = a_{r,n1}, \\ a_{u,0m} &= a_{d,1m}, a_{d,N_y+1m} = a_{u,N_ym}. \end{aligned} \tag{SM41}$$

Due to the translational symmetry of the network on torus and cylinder, the solution has the form

$$\begin{pmatrix} a_{r,nm} \\ a_{u,nm} \\ a_{l,nm} \\ a_{d,nm} \end{pmatrix} = \frac{1}{\sqrt{N_x}} e^{ik_x m} \begin{pmatrix} a_{r,n} \\ a_{u,n} \\ a_{l,n} \\ a_{d,n} \end{pmatrix}, \tag{SM42}$$

with the quasi-momentum $k_x = -\pi + 2\pi n/N_x$ ($n = 0, 1, 2, ..., N_x - 1$), and the scattering Eq. (SM36) becomes

$$S_0(k_x) \begin{pmatrix} a_{r,n} \\ a_{u,n} \\ a_{l,n} \\ a_{d,n} \end{pmatrix} = e^{-i\mathcal{E}L} e^{i\frac{\chi}{N_x}\mathcal{N}_n L} \begin{pmatrix} a_{r,n} \\ a_{u,n-1} \\ a_{l,n} \\ a_{d,n+1} \end{pmatrix}. \tag{SM43}$$

where

$$S_0(k_x) = \frac{1}{\sqrt{2}} \begin{pmatrix} 0 & ie^{-ik_x} e^{-in\sigma\theta_0} & 0 & e^{-ik_x} e^{-in\sigma\theta_0} \\ i & 0 & 1 & 0 \\ 0 & e^{ik_x} e^{in\sigma\theta_0} & 0 & ie^{ik_x} e^{in\sigma\theta_0} \\ 1 & 0 & i & 0 \end{pmatrix}, \tag{SM44}$$

and the intensity matrix

$$\mathcal{N}_n = \begin{pmatrix} |a_{r,n}|^2 + 2|a_{l,n}|^2 & 0 & 0 & 0 \\ 0 & |a_{u,n-1}|^2 + 2|a_{d,n}|^2 & 0 & 0 \\ 0 & 0 & |a_{l,n}|^2 + 2|a_{r,n}|^2 & 0 \\ 0 & 0 & 0 & |a_{d,n+1}|^2 + 2|a_{u,n}|^2 \end{pmatrix}. \tag{SM45}$$

By taking into account the boundary conditions (SM39) and (SM40), the scattering equation for the entire network on the torus and the cylinder can be symbolically written as

$$S_0(k_x)\mathbf{a} = e^{-i\mathcal{E}L} e^{i\frac{\chi}{N_x}\mathcal{N}_n L}\mathbf{a} \tag{SM46}$$

in the basis $\mathbf{a} = (a_{r,1}, ..., a_{r,N_y}; a_{u,1}, ..., a_{u,N_y}; a_{l,1}, ..., a_{l,N_y}; a_{d,1}, ..., a_{d,N_y})^T$. Similarly, by the boundary condition (SM41), the scattering equation for the planar network reads

$$S_0\mathbf{a} = e^{-i\mathcal{E}L} e^{i\chi\mathcal{N}L}\mathbf{a} \tag{SM47}$$

in the basis $\mathbf{a} = (a_{r,11}, ..., a_{r,N_yN_x}; a_{u,11}, ..., a_{u,N_yN_x}; a_{l,11}, ..., a_{l,N_yN_x}; a_{d,11}, ..., a_{d,N_yN_x})^T$.

In the main text, we numerically solve Eqs. (SM46) and (SM47) for the linear closed network, i.e., $\chi = 0$, and show the spectra $\mathcal{E}$ of the network with different geometries in Fig. 2 and 3. For the closed nonlinear network, i.e., $\chi \neq 0$, the solutions are unstable in general. In order to generate and stablize the state of light with Kerr nonlinearities, we drive the network through the top boundary mirrors of cylindrical open network.

SMIIIB-Open network

For the open network on the cylinder shown in Fig. SM3a, we drive the network through the top boundary mirrors of the reflection (transmission) coefficient r_{BM} (t_{BM}), where the driving light with frequency ω_{d} has the amplitude $A^{(0)}_{\mathrm{in},m}$.

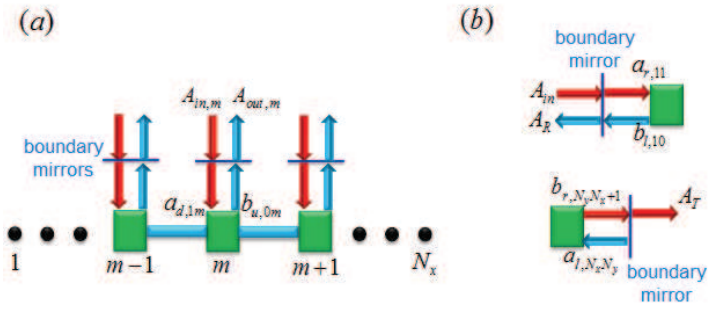

FIG. SM3: (Color Online) The schematic for the boundary mirrors in the cylindrical and planar networks: (a) Driven cylindrical network through each of the partially transmissive mirrors on the top boundary. (b) Light reflection and transmission through the boundary mirrors next to the nodes $(1,1)$ and (N_y, N_x) in the planar network (i.e., nodes in the upper left and lower right corners of the planar network).

The S-matrix

$$S_{\rm BM} = \begin{pmatrix} t_{\rm BM} & ir_{\rm BM} \\ ir_{\rm BM} & t_{\rm BM} \end{pmatrix} \tag{SM48}$$

of transmissive mirrors results in the boundary condition

$$S_{\rm BM} \begin{pmatrix} A^{(0)}_{{\rm in},m} \\ b_{u,0m} e^{i\omega_{\rm d} L/2} \end{pmatrix} = \begin{pmatrix} a_{d,1m} e^{-i\omega_{\rm d} L/2} \\ A^{(0)}_{{\rm out},m} \end{pmatrix}, \tag{SM49}$$

where $A^{(0)}_{{\rm in},m}$ and $A^{(0)}_{{\rm out},m}$ are the amplitudes of input and output fields above boundary mirrors (Fig. SM3a), and $a_{d,1m}$ and $b_{u,0m}$ are the amplitudes of the down-moving input field and the up-moving output field at the top of the cylinder (i.e., the boundary nodes $(1,m)$). For the driving amplitude $A^{(0)}_{{\rm in},m} = A^{(0)}_{\rm in} e^{ik_x m}/\sqrt{N_x}$ with the quasi-momentum k_x, the boundary condition becomes

$$S_{\rm BM} \begin{pmatrix} A^{(0)}_{\rm in} \\ b_{u,0} e^{i\omega_{\rm d} L/2} \end{pmatrix} = \begin{pmatrix} a_{d,1} e^{-i\omega_{\rm d} L/2} \\ A^{(0)}_{\rm out} \end{pmatrix}, \tag{SM50}$$

where we used $a_{d,1m} = a_{d,1} e^{ik_x m}/\sqrt{N_x}$, $b_{u,0m} = b_{u,0} e^{ik_x m}/\sqrt{N_x}$, and $A^{(0)}_{{\rm out},m} = A^{(0)}_{\rm out} e^{ik_x m}/\sqrt{N_x}$. The scattering equation of the open cylindrical network reads

$$R_{\rm BM} S_0(k_x)\mathbf{a} = e^{-i\omega_{\rm d} L} e^{i\frac{\chi}{N_x}\mathcal{N}_n L}\mathbf{a} - t_{\rm BM} e^{-i\omega_{\rm d} L/2}\mathbf{A}^{(0)}_{\rm in}, \tag{SM51}$$

where $R_{\rm BM}$ is obtained by replacing the diagonal matrix element $I_{3N_y+1,3N_y+1}$ of the $4N_y$-dimensional identity matrix I by $ir_{\rm BM}$, and $\mathbf{A}^{(0)}_{\rm in} = A^{(0)}_{\rm in}(\mathbf{0};\mathbf{0};\mathbf{0};\mathbf{1})^T$ is composed of the null vector $\mathbf{0}$ and $\mathbf{1} = (1,0,...,0)$, which are of dimension N_y. The solution of the scattering Eq. (SM51) determines the out-going amplitude

$$A^{(0)}_{\rm out} = \frac{t_{\rm BM}}{ir_{\rm BM}} e^{-i\omega_{\rm d} L/2} a_{d,1} - \frac{A^{(0)}_{\rm in}}{ir_{\rm BM}}. \tag{SM52}$$

When the driving frequency $\omega_{\rm d}$ is resonant with the eigenfrequency $\mathcal{E}$ of the closed system, the boundary condition (SM50) leads to the amplitude

$$a_{d,1} = \frac{t_{\rm BM}}{1 - ir_{\rm BM}} A^{(0)}_{\rm in} e^{i\omega_{\rm d} L/2}, \tag{SM53}$$

and the input-output relation $A^{(0)}_{\rm out} = e^{i\delta_0} A^{(0)}_{\rm in}$ with the phase shift

$$\delta_0 = \arg\left(\frac{1 + ir_{\rm BM}}{1 - ir_{\rm BM}}\right). \tag{SM54}$$

In the main text, we consider linear and nonlinear open networks on the cylindrical geometry. In the linear case, we study the detection of the energy spectrum through the phase shift δ_0. In the nonlinear case, we numerically solve Eq. (SM51) for the network with size 24×12, and show the light distributions for different k_x and $\omega_{\rm d}$ in Fig. 4.

For the open network on the plane shown in Fig. SM3b, we drive the network through the boundary mirror next to the node $(1,1)$ by the light with frequency $\omega_{\rm d}$, and detect the transimission to the node (N_x, N_y).

The S-matrix (SM48) of two transmissive mirrors (see Fig. SM3b) gives the boundary conditions

$$\begin{aligned} S_{\rm BM}\begin{pmatrix} A_{\rm in}^{(0)} \\ b_{l,10}e^{i\omega_{\rm d}L/2}\end{pmatrix} &= \begin{pmatrix} a_{r,11}e^{-i\omega_{\rm d}L/2} \\ A_{\rm R}\end{pmatrix}, \\ S_{\rm BM}\begin{pmatrix} b_{r,N_yN_x+1}e^{i\omega_{\rm d}L/2} \\ 0\end{pmatrix} &= \begin{pmatrix} A_{\rm T} \\ a_{l,N_yN_x}e^{-i\omega_{\rm d}L/2}\end{pmatrix}, \end{aligned} \tag{SM55}$$

where $A_{\rm in}^{(0)}$ denotes the input amplitude of the network, and $A_{\rm R}$ ($A_{\rm T}$) are the reflection (transmission) amplitude. The amplitudes of right-moving input and left-moving output fields at the node $(1,1)$ are $a_{r,11}$ and $b_{l,10}$, while the amplitudes of left-moving input and right-moving output fields at nodes (N_x, N_y) are a_{l,N_yN_x} and b_{r,N_yN_x+1}. The scattering equation of the open network on the plane reads

$$\bar{R}_{\rm BM}S_0\mathbf{a} = e^{-i\omega_{\rm d}L}e^{i\chi\mathcal{N}L}\mathbf{a} - t_{\rm BM}e_{\rm in}^{-i\omega_{\rm d}L/2}\mathbf{A}_{\rm in}^{(0)}, \tag{SM56}$$

where $\bar{R}_{\rm BM}$ is obtained by replacing the diagonal matrix elements $I_{1,1}$ and $I_{3N_xN_y,3N_xN_y}$ of the $4N_xN_y$-dimensional identity matrix I by $ir_{\rm BM}$, and $\mathbf{A}_{\rm in}^{(0)} = A_{\rm in}^{(0)}(\mathbf{1};\mathbf{0};\mathbf{0};\mathbf{0})^T$ is composed of the null vector $\mathbf{0}$ and $\mathbf{1} = (1,0,...,0)$, which are of dimension N_xN_y. The solution of the scattering Eq. (SM56) determines the reflection and transmission amplitudes

$$\begin{aligned} A_{\rm R} &= \frac{t_{\rm BM}}{ir_{\rm BM}}a_{r,11}e^{-i\omega_{\rm d}L/2} - \frac{A_{\rm in}^{(0)}}{ir_{\rm BM}}, \\ A_{\rm T} &= \frac{t_{\rm BM}}{ir_{\rm BM}}a_{l,N_yN_x}e^{-i\omega_{\rm d}L/2}. \end{aligned} \tag{SM57}$$

In the main text, we study the light transmission to the linear network on the open plane by solving Eq. (SM56). The solution of Eq. (SM56) determines the light distribution in the network, and $\left|A_{\rm T}/A_{\rm in}^{(0)}\right|^2$ is the transmission probability, which are shown in Fig. 3b for different driving frequency $\omega_{\rm d}$.

SMIV-BOGOLIUBOV EXCITATIONS

In this section, we study the response of the cylindrical network to small input fluctuations, where the total input field

$$A_m^{\rm in}(t) = [A_{{\rm in},m}^{(0)} + \delta A_m^{\rm in}(t)]e^{-i\omega_{\rm d}t} \tag{SM58}$$

contains a small probe field

$$\delta A_m^{\rm in}(t) = \frac{1}{\sqrt{N_x}}[\delta A_{\rm in}^{(+)}e^{ip_xm}e^{-i\omega_{\rm f}t} + \delta A_{\rm in}^{(-)}e^{i(2k_x-p_x)m}e^{i\omega_{\rm f}t}] \tag{SM59}$$

with frequency $\omega_{\rm f}$ around the driving field $A_m^{\rm in}$ that generates the steady state.

As discussed in Sec. SMIIA, the motion equations

$$i\partial_t\delta\Psi_H + \mathbf{\Sigma}\partial_x\delta\Psi_H = \mathbf{M}_H\delta\Psi_H, \tag{SM60}$$

and

$$i\partial_t\delta\Psi_V + \mathbf{\Sigma}\partial_x\delta\Psi_V = \mathbf{M}_V\delta\Psi_V \tag{SM61}$$

describe the dynamics of Bogoliubov fluctuations $\delta\Psi_H = (\delta\phi_{r,nm}, \delta\phi_{l,nm-1}, \delta\phi_{r,nm}^*, \delta\phi_{l,nm-1}^*)^T$ and $\delta\Psi_V = (\delta\phi_{u,nm}, \delta\phi_{d,n+1m}, \delta\phi_{u,nm}^*, \delta\phi_{d,n+1m}^*)^T$ in the horizontal and vertical fibers, respectively. The probe field (SM59) induces the fluctuation field with the configurations

$$\delta\phi_{s,nm}(x,t) = \frac{1}{\sqrt{N_x}}[\delta\psi_{s,n,p_x}(x)e^{ip_xm}e^{-i\omega_{\rm f}t} + \delta\psi_{s,n,q_x}(x)e^{iq_xm}e^{i\omega_{\rm f}t}], \tag{SM62}$$

where $q_x = 2k_x - p_x$ and the subindex $s = r, u, l, d$. The relations (SM13) and (SM18) become

$$\bar{P}_H \begin{pmatrix} e^{-in\sigma\theta_0}\delta b_{r,n,p_x} \\ e^{-in\sigma\theta_0}\delta a_{l,n,p_x} \\ e^{in\sigma\theta_0}\delta b^*_{r,n,q_x} \\ e^{in\sigma\theta_0}\delta a^*_{l,n,q_x} \end{pmatrix} = \begin{pmatrix} \delta a_{r,n,p_x} \\ \delta b_{l,n,p_x} \\ \delta a^*_{r,n,q_x} \\ \delta b^*_{l,n,q_x} \end{pmatrix}, \tag{SM63}$$

and

$$\bar{P}_V \begin{pmatrix} \delta b_{u,n,p_x} \\ \delta a_{d,n+1,p_x} \\ \delta b^*_{u,n,q_x} \\ \delta a^*_{d,n+1,q_x} \end{pmatrix} = \begin{pmatrix} \delta a_{u,n,p_x} \\ \delta b_{d,n+1,p_x} \\ \delta a^*_{u,n,q_x} \\ \delta b^*_{d,n+1,q_x} \end{pmatrix}, \tag{SM64}$$

where the input and output fields at the nodes are

$$\begin{aligned} \delta a_{r,n,p_x} &= \delta\psi_{r,n,p_x}(L), \delta a_{l,n,p_x} = e^{in\sigma\theta_0}\delta\psi_{l,n,p_x}(0), \\ \delta b_{r,n,p_x} &= e^{in\sigma\theta_0}\delta\psi_{r,n,p_x}(0), \delta b_{l,n,p_x} = \delta\psi_{l,n,p_x}(L), \\ \delta a_{u,n,p_x} &= \delta\psi_{u,n,p_x}(L), \delta a_{d,n+1,p_x} = \delta\psi_{d,n+1,p_x}(0), \\ \delta b_{u,n,p_x} &= \delta\psi_{u,n,p_x}(0), \delta b_{d,n+1,p_x} = \delta\psi_{d,n+1,p_x}(L). \end{aligned} \tag{SM65}$$

The propagation matrices $\bar{P}_H = e^{\mathbf{\Sigma}(\omega_\mathrm{f} - \bar{\mathbf{M}}_H)L}$ and $\bar{P}_V = e^{\mathbf{\Sigma}(\omega_\mathrm{f} - \bar{\mathbf{M}}_V)L}$ are determined by

$$\bar{\mathbf{M}}_H = \frac{\chi}{N_x} \begin{pmatrix} |a_{r,n}|^2 & 2e^{i(k_x-p_x)}\tilde{a}^*_{l,n}a_{r,n} & a^2_{r,n} & 2e^{i(k_x-p_x)}a_{r,n}\tilde{a}_{l,n} \\ 2e^{-i(k_x-p_x)}a^*_{r,n}\tilde{a}_{l,n} & |\tilde{a}_{l,n}|^2 & 2e^{-i(k_x-p_x)}a_{r,n}\tilde{a}_{l,n} & \tilde{a}^2_{l,n} \\ -a^{*2}_{r,n} & -2e^{i(k_x-p_x)}a^*_{r,n}\tilde{a}^*_{l,n} & -|a_{r,n}|^2 & -2e^{i(k_x-p_x)}a^*_{r,n}\tilde{a}_{l,n} \\ -2e^{-i(k_x-p_x)}a^*_{r,n}\tilde{a}^*_{l,n} & -\tilde{a}^{*2}_{l,n} & -2e^{-i(k_x-p_x)}\tilde{a}^*_{l,n}a_{r,n} & -|\tilde{a}_{l,n}|^2 \end{pmatrix}, \tag{SM66}$$

and

$$\bar{\mathbf{M}}_V = \frac{\chi}{N_x} \begin{pmatrix} |a_{u,n}|^2 & 2a^*_{d,n+1}a_{u,n} & a^2_{u,n} & 2a_{u,n}a_{d,n+1} \\ 2a^*_{u,n}a_{d,n+1} & |a_{d,n+1}|^2 & 2a_{u,n}a_{d,n+1} & a^2_{d,n+1} \\ -a^{*2}_{u,n} & -2a^*_{u,n}a^*_{d,n+1} & -|a_{u,n}|^2 & -2a^*_{u,n}a_{d,n+1} \\ -2a^*_{u,n}a^*_{d,n+1} & -a^{*2}_{d,n+1} & -2a^*_{d,n+1}a_{u,n} & -|a_{d,n+1}|^2 \end{pmatrix} \tag{SM67}$$

in the horizontal and vertical fibers, respectively, where $\tilde{a}_{l,n} = e^{-in\sigma\theta_0}a_{l,n}$.

The relations between the input δa and output fields δb at the nodes follow from Eqs. (SM63) and (SM64) as

$$\begin{pmatrix} \bar{P}_{H,11}e^{-in\sigma\theta_0} & 0 & \bar{P}_{H,13}e^{in\sigma\theta_0} & 0 \\ -\bar{P}_{H,21}e^{-in\sigma\theta_0} & 1 & -\bar{P}_{H,23}e^{in\sigma\theta_0} & 0 \\ \bar{P}_{H,31}e^{-in\sigma\theta_0} & 0 & \bar{P}_{H,33}e^{in\sigma\theta_0} & 0 \\ -\bar{P}_{H,41}e^{-in\sigma\theta_0} & 0 & -\bar{P}_{H,43}e^{in\sigma\theta_0} & 1 \end{pmatrix} \begin{pmatrix} \delta b_{r,n,p_x} \\ \delta b_{l,n,p_x} \\ \delta b^*_{r,n,q_x} \\ \delta b^*_{l,n,q_x} \end{pmatrix} = \begin{pmatrix} 1 & -\bar{P}_{H,12}e^{-in\sigma\theta_0} & 0 & -\bar{P}_{H,14}e^{in\sigma\theta_0} \\ 0 & \bar{P}_{H,22}e^{-in\sigma\theta_0} & 0 & \bar{P}_{H,24}e^{in\sigma\theta_0} \\ 0 & -\bar{P}_{H,32}e^{-in\sigma\theta_0} & 1 & -\bar{P}_{H,34}e^{in\sigma\theta_0} \\ 0 & \bar{P}_{H,42}e^{-in\sigma\theta_0} & 0 & \bar{P}_{H,44}e^{in\sigma\theta_0} \end{pmatrix} \begin{pmatrix} \delta a_{r,n,p_x} \\ \delta a_{l,n,p_x} \\ \delta a^*_{r,n,q_x} \\ \delta a^*_{l,n,q_x} \end{pmatrix}, \tag{SM68}$$

and

$$\begin{pmatrix} \bar{P}_{V,11} & 0 & \bar{P}_{V,13} & 0 \\ -\bar{P}_{V,21} & 1 & -\bar{P}_{V,23} & 0 \\ \bar{P}_{V,31} & 0 & \bar{P}_{V,33} & 0 \\ -\bar{P}_{V,41} & 0 & -\bar{P}_{V,43} & 1 \end{pmatrix} \begin{pmatrix} \delta b_{u,n,p_x} \\ \delta b_{d,n+1,p_x} \\ \delta b^*_{u,n,q_x} \\ \delta b^*_{d,n+1,q_x} \end{pmatrix} = \begin{pmatrix} 1 & -\bar{P}_{V,12} & 0 & -\bar{P}_{V,14} \\ 0 & \bar{P}_{V,22} & 0 & \bar{P}_{V,24} \\ 0 & -\bar{P}_{V,32} & 1 & -\bar{P}_{V,34} \\ 0 & \bar{P}_{V,42} & 0 & \bar{P}_{V,44} \end{pmatrix} \begin{pmatrix} \delta a_{u,n,p_x} \\ \delta a_{d,n+1,p_x} \\ \delta a^*_{u,n,q_x} \\ \delta a^*_{d,n+1,q_x} \end{pmatrix}. \tag{SM69}$$

Equations (SM68) and (SM69) give the relation

$$\begin{pmatrix} \delta b \\ \delta b^* \end{pmatrix} = H_\mathrm{f}(\omega_\mathrm{f}) \begin{pmatrix} \delta a \\ \delta a^* \end{pmatrix} \tag{SM70}$$

On the other hand, the S-matrix S_node leads to the input-output relation

$$S_{f,\mathrm{node}}(p_x) \begin{pmatrix} \delta a_{r,n,p_x} \\ \delta a_{u,n,p_x} \\ \delta a_{l,n,p_x} \\ \delta a_{d,n,p_x} \end{pmatrix} = \begin{pmatrix} e^{ip_x}\delta b_{r,n,p_x} \\ \delta b_{u,n-1,p_x} \\ e^{-ip_x}\delta b_{l,n,p_x} \\ \delta b_{d,n+1,p_x} \end{pmatrix} \tag{SM71}$$

at each node, where

$$S_{f,\mathrm{node}}(p_x) = e^{i\omega_\mathrm{d} L} e^{-i\frac{\chi}{N_x}\mathcal{N}_n L} \begin{pmatrix} e^{-ip_x} & 0 & 0 & 0 \\ 0 & 1 & 0 & 0 \\ 0 & 0 & e^{ip_x} & 0 \\ 0 & 0 & 0 & 1 \end{pmatrix} S_\mathrm{node}. \tag{SM72}$$

The S-matrix S_BM of transmissive mirrors at the top of the cylinder give the boundary condition

$$\begin{aligned} ir_\mathrm{BM}\delta b_{u,0,p_x} &= e^{-i\omega_\mathrm{f} L}\delta a_{d,1,p_x} - t_\mathrm{BM}\delta A_\mathrm{in}^{(+)} e^{i(\omega_\mathrm{d}-\omega_\mathrm{f})\frac{L}{2}}, \\ ir_\mathrm{BM}\delta b_{u,0,q_x} &= e^{i\omega_\mathrm{f} L}\delta a_{d,1,q_x} - t_\mathrm{BM}\delta A_\mathrm{in}^{(-)} e^{i(\omega_\mathrm{d}+\omega_\mathrm{f})\frac{L}{2}}. \end{aligned} \tag{SM73}$$

and the components

$$\begin{aligned} \delta A_\mathrm{out}^{(+)} &= \frac{t_\mathrm{BM}}{ir_\mathrm{BM}} e^{-i(\omega_\mathrm{d}+\omega_\mathrm{f})\frac{L}{2}}\delta a_{d,1,p_x} - \frac{\delta A_\mathrm{in}^{(+)}}{ir_\mathrm{BM}}, \\ \delta A_\mathrm{out}^{(-)} &= \frac{t_\mathrm{BM}}{ir_\mathrm{BM}} e^{-i(\omega_\mathrm{d}-\omega_\mathrm{f})\frac{L}{2}}\delta a_{d,1,q_x} - \frac{\delta A_\mathrm{in}^{(-)}}{ir_\mathrm{BM}}. \end{aligned} \tag{SM74}$$

of positive and negative frequencies in the output fluctuation field

$$\delta A_m^\mathrm{out}(t) = \frac{1}{\sqrt{N_x}}[\delta A_\mathrm{out}^{(+)} e^{ip_x m} e^{-i\omega_\mathrm{f} t} + \delta A_\mathrm{out}^{(-)} e^{iq_x m} e^{i\omega_\mathrm{f} t}] \tag{SM75}$$

around the output field A_m^out in the steady state.

By the elimination of the output fluctuation fields $\delta b_{s,n,p_x(q_x)}$ in Eqs. (SM70), (SM71), and the boundary condition (SM73), we establish the scattering equation

$$\mathbf{D}(\omega_\mathrm{f}) \begin{pmatrix} \delta\mathbf{a}_{p_x} \\ \delta\mathbf{a}_{q_x}^* \end{pmatrix} = t_\mathrm{BM} \begin{pmatrix} \delta\mathbf{A}_\mathrm{in}^{(+)} e^{i(\omega_\mathrm{d}-\omega_\mathrm{f})\frac{L}{2}} \\ \delta\mathbf{A}_\mathrm{in}^{(-)*} e^{-i(\omega_\mathrm{d}+\omega_\mathrm{f})\frac{L}{2}} \end{pmatrix} \tag{SM76}$$

of Bogoliubov fluctuations by the matrix

$$\mathbf{D}(\omega_\mathrm{f}) = H_\mathrm{f}(\omega_\mathrm{f}) - \begin{pmatrix} S_{f,\mathrm{node}}(p_x) & 0 \\ 0 & S_{f,\mathrm{node}}^*(q_x) \end{pmatrix}, \tag{SM77}$$

where $\delta\mathbf{a}_{p_x} = (\delta a_{r,n,p_x}, \delta a_{u,n,p_x}, \delta a_{l,n,p_x}, \delta a_{d,n,p_x})^T$, and $\delta\mathbf{A}_\mathrm{in}^{(\pm)} = \delta A_\mathrm{in}^{(\pm)}(\mathbf{0};\mathbf{0};\mathbf{0};\mathbf{1})$ is composed of the null vector $\mathbf{0}$ and $\mathbf{1} = (1, 0, ..., 0)$, which are of dimension N_y. The steady-state is stable if all roots $\mathcal{E}_f$ of $\det\mathbf{D}(\omega_\mathrm{f})$ satisfy $\mathrm{Im}\mathcal{E}_f < 0$. For $\omega_\mathrm{d} = 0.22$ and $\omega_\mathrm{d} = 4.5\times10^{-2}$, we mark the stable regimes by the black dots in the χN_p versus $\chi\left|A_\mathrm{in}^{(0)}\right|^2$ curves of Fig. SM4, where $k_x = 0.26$ and $r_\mathrm{BM} = 0.9$.

The solutions $(\delta\mathbf{a}_{p_x}, \delta\mathbf{a}_{q_x}^*)$ of Eq. (SM76) lead to the input-output relation

$$\begin{pmatrix} \delta A_\mathrm{out}^{(+)} \\ \delta A_\mathrm{out}^{(-)*} \end{pmatrix} = M_\mathrm{IO} \begin{pmatrix} \delta A_\mathrm{in}^{(+)} \\ \delta A_\mathrm{in}^{(-)*} \end{pmatrix} \tag{SM78}$$

by Eqs. (SM74), where the 2×2 matrix

$$M_\mathrm{IO} = \frac{1}{ir_\mathrm{BM}}\sigma_z[t_\mathrm{BM}^2 e^{-i\omega_\mathrm{f} L} e^{-i\omega_\mathrm{d}\frac{L}{2}\sigma_z}\tilde{D}(\omega) e^{i\omega_\mathrm{d}\frac{L}{2}\sigma_z} - I_2] \tag{SM79}$$

is determined by

$$\tilde{D}(\omega) = \begin{pmatrix} [\mathbf{D}^{-1}(\omega)]_{3N_y+1,3N_y+1} & [\mathbf{D}^{-1}(\omega)]_{3N_y+1,7N_y+1} \\ [\mathbf{D}^{-1}(\omega)]_{7N_y+1,3N_y+1} & [\mathbf{D}^{-1}(\omega)]_{7N_y+1,7N_y+1} \end{pmatrix}. \tag{SM80}$$

By using the input-output matrix M_IO, we investigate the reflection fields with the positive and negative frequencies under the driving positive frequency field ($\delta A_\mathrm{in}^{(-)} = 0$). The components $(M_\mathrm{IO})_{11}$ and $(M_\mathrm{IO})_{21}$ determine the squeezing spectra shown in Fig. 5a of the main text. By solving Eq. (SM76), in Fig. 5b of the main text, we show the light distributions of Bogoliubov fluctuations around steady states.

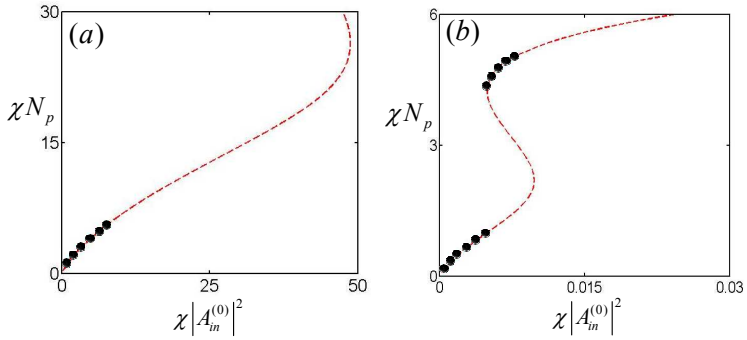

FIG. SM4: (Color Online) For $k_x = 0.26$ and $r_{\mathrm{BM}} = 0.9$, the stable regimes are shown by the black dots in the χN_p versus $\chi\left|A_{\mathrm{in}}^{(0)}\right|^2$ curves, where $\omega_{\mathrm{d}} = 0.22$ (a) and $\omega_{\mathrm{d}} = 4.5 \times 10^{-2}$ (b).